




# Switchable large-gap quantum spin Hall state in the two-dimensional $MSi_2Z_4$ class of materials

Rajibul Islam,<sup>1,2,\*</sup> Rahul Verma,<sup>2</sup> Barun Ghosh,<sup>3</sup> Zahir Muhammad <sup>1,4</sup> Arun Bansil,<sup>3</sup>  
Carmino Autieri <sup>1,5,†</sup> and Bahadur Singh <sup>2,‡</sup>

<sup>1</sup>International Research Centre MagTop, Institute of Physics, Polish Academy of Sciences, Aleja Lotników 32/46, PL-02668 Warsaw, Poland

<sup>2</sup>Department of Condensed Matter Physics and Materials Science, Tata Institute of Fundamental Research, Colaba, Mumbai 400005, India

<sup>3</sup>Department of Physics, Northeastern University, Boston, Massachusetts 02115, USA

<sup>4</sup>Hefei Innovation Research Institute, School of Microelectronics, Beihang University, Hefei 230013, People's Republic of China

<sup>5</sup>Consiglio Nazionale delle Ricerche CNR-SPIN, UOS Salerno, I-84084 Fisciano (Salerno), Italy



(Received 26 July 2022; accepted 1 December 2022; published 29 December 2022)

Quantum spin Hall (QSH) insulators exhibit spin-polarized conducting edge states that are topologically protected from backscattering and offer unique opportunities to address fundamental science questions and device applications. Finding viable materials that host such topological states, however, remains a continuing challenge. Here, by using in-depth first-principles theoretical modeling, we predict large band gap QSH insulators in the recently synthesized bottom-up two-dimensional  $MSi_2Z_4$  ( $M = \text{Mo}$  or  $\text{W}$  and  $Z = \text{P}$  or  $\text{As}$ ) material family with  $1T'$  structure. A structural distortion in the  $2H$  phase drives a band inversion between the metal ( $\text{Mo}/\text{W}$ )  $d$  and  $p$  states of  $\text{P}/\text{As}$  to realize spinless Dirac states without spin-orbit coupling. When spin-orbit coupling is included, a hybridization gap as large as  $\sim 204$  meV opens up at the band-crossing points, realizing spin-polarized conducting edge states with nearly quantized spin Hall conductivity. We also show that the inverted band gap can be tuned with a vertical electric field, which drives a topological phase transition from the QSH to a trivial insulator with Rashba-like edge states. Our study identifies the two-dimensional  $MSi_2Z_4$  material family in the  $1T'$  structure as large band gap, tunable QSH insulators with protected spin-polarized edge states and large spin Hall conductivity.

DOI: [10.1103/PhysRevB.106.245149](https://doi.org/10.1103/PhysRevB.106.245149)

## I. INTRODUCTION

Following the early studies of two-dimensional (2D) materials [1–4], Kane and Mele demonstrated the existence of a quantum spin Hall (QSH) state in graphene in the presence of symmetry-allowed spin-orbit coupling (SOC) [5,6]. The QSH state features one-dimensional (1D) conducting helical edge modes in insulating bulk due to the nontrivial winding of their electronic states [5–13]. The helical edge modes carry symmetry-protected spin-polarized electronic states that hold immense potential for designing high-efficiency quantum electronic devices with low dissipation [14–16]. The QSH state has been theoretically predicted in a variety of 2D materials and quantum well structures. However, its experimental realization has so far been demonstrated only in  $\text{HgTe}/\text{CdTe}$  and  $\text{InAs}/\text{GaSb}$  quantum wells and thin films of  $1T'$ - $\text{WTe}_2$ ,  $\text{HgPt}_2\text{Se}_3$ , and  $\text{Bi}_4\text{Br}_4$  at ultralow temperatures [17–23]. A common approach to realize the QSH state is to reduce the thickness of three-dimensional (3D)  $Z_2$  topological insulators to drive a 3D to 2D crossover and a band inversion in the surface states. This method has successfully predicted the QSH state in thin films of  $Z_2$  topological insulators [12,13,24–27]. The process of fine tuning quantum well structures or

manipulating film thickness to generate an inverted hybridization gap in the surface spectrum [12,13,24–31], however, can modify material properties, leading to complicated electronic structures and quenching of the quantized spin Hall conductance. It is important, therefore, to look for new strategies for designing 2D materials with large inverted band gaps in which the QSH state can survive at room temperature.

Here, we present an in-depth first-principles analysis with optimized crystal structures to demonstrate the presence of the QSH state in recently introduced 2D materials that can be realized via a bottom-up approach without parental analogs [32–34]. These synthetic 2D materials provide an emerging paradigm for engineering designer states with diverse functionalities. Specifically, 2D  $\text{MoSi}_2\text{N}_4$  materials were synthesized by passivating high-energy surfaces of nonlayered nitrides with Si with remarkable stability under ambient conditions [34]. They show semiconducting behavior with high carrier mobility and feature spin-valley locking, gating and thickness-tunable spin polarization, and 2D magnetism and a correlation-driven quantum anomalous Hall state, among other properties depending on their compositions [35–38]. Theoretically predicted properties of these materials are reported to be superior to those of the widely used 2D transition metal dichalcogenides (TMDs) [34,35,39,40]. It is not clear, however, if these materials can form polytypic structures and realize a QSH state similar to the 2D TMDs. Here, based on our molecular dynamics simulations and phonon calculations, we predict that the  $1T'$  phase of  $MSi_2Z_4$  ( $M = \text{Mo}$  or  $\text{W}$

\*rislam@magtop.ifpan.edu.pl

†autieri@magtop.ifpan.edu.pl

‡bahadur.singh@tifr.res.in

and  $Z = \text{P}$  or  $\text{As}$ ) is stable and realizes a QSH state via a structural distortion from the  $2H$  to  $1T'$  phase. Our calculated inverted band gap ( $\sim 204$  meV) and spin Hall conductivity (SHC;  $\sim 1.3e^2/h$ ) are higher than the top-to-bottom grown 2D TMDs. We also show that the QSH state of  $MSi_2Z_4$  can be switched off by driving a topological phase transition via an applied (vertical) electric field. Our study indicates the robust presence of a switchable QSH state in a polytypic structure of bottom-up grown 2D materials with excellent topological and spintronics properties.

## II. METHODOLOGY

Electronic structure calculations were performed within the framework of the density functional theory based on the projector augmented wave method using the VASP [41,42] code. The self-consistent relativistic calculations were performed with a plane wave cutoff energy of 500 eV and a  $\Gamma$ -centered  $6 \times 12 \times 1$   $k$  mesh for Brillouin zone (BZ) sampling. We used the generalized gradient approximation (GGA) to include exchange-correlation effects [43]. The structural parameters were fully optimized until the residual forces on each atom were less than  $0.001$  eV/Å and the total energy was converged to  $10^{-8}$  eV. For a more accurate treatment of electronic correlations, we also employed the Heyd-Scuseria-Ernzerhof (HSE) hybrid functional with 25% exact Hartree-Fock exchange [44]. Phonon dispersions were calculated with the density functional perturbation theory using the PHONOPY code [45] with a  $2 \times 4 \times 1$  supercell. The *ab initio* molecular dynamics simulations were performed with a Nosé-Hoover thermostat at a constant temperature of 300 K with a time step of 2 fs [46]. We generated material-specific tight-binding Hamiltonians with  $M$   $d$ , Si  $s$  and  $p$ , and  $Z$   $p$  orbitals using the VASP2WANNIER interface [47], which was also used to elucidate topological properties using the WANNIERTOOLS package [48,49].

## III. RESULTS AND DISCUSSION

### A. Structural properties

The pristine phase of monolayer  $MSi_2Z_4$  belongs to the  $1H$  crystal structure family of 2D materials with space group  $D_{3h}^1$  ( $P\bar{6}m2$ , No. 187) [34,35]. Figure 1(a) shows the crystal lattice of  $MoSi_2P_4$  as an exemplar system. The structure is layered along the hexagonal  $c$  axis and consists of  $MoP_2$  layers sandwiched between two  $SiP$  layers. The Mo atoms are located at the center of the trigonal prismatic building block with six P atoms and the  $MoP_2$  layer bonded vertically with the  $SiP$  layer [34]. In the  $1T'$  phase of  $MoSi_2P_4$  [Fig. 1(b)], the three atomic layers are locked in such a way that the position of Mo atoms is at the center of a  $60^\circ$  twisted trigonal prismatic building block with six P atoms. This creates the octahedral local coordination of Mo atoms with the six P atoms in the  $MoP_2$  layer but with different Mo-Mo bond lengths to form zigzag atomic chains along the  $y$  axis and period doubling along the  $x$  axis. This structural distortion lowers the hexagonal  $1H$  symmetry to  $1T'$  monoclinic symmetry with space group  $P2_1/m$  (No. 11) and forms a rectangular primitive unit cell, as shown in Fig. 1(b). Importantly, the  $1T'$  structure possesses the inversion symmetry  $I$ , in contrast to the  $1H$

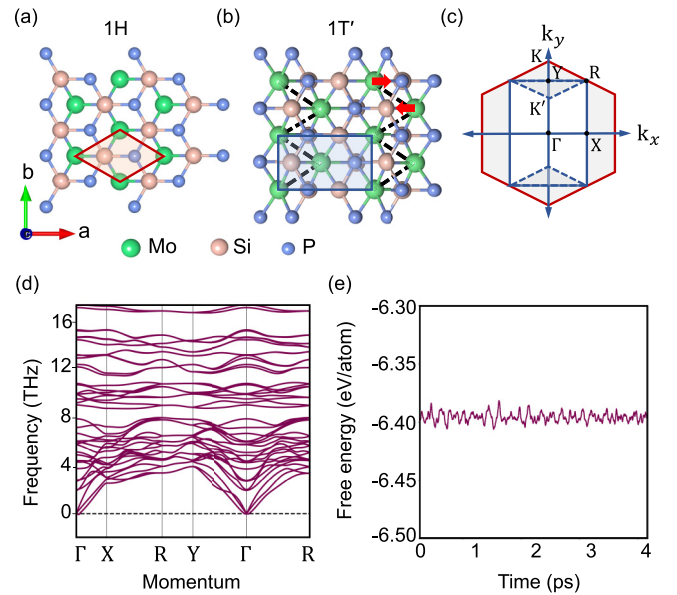


FIG. 1. Crystal structure of a  $MoSi_2P_4$  monolayer in the (a)  $1H$  and (b)  $1T'$  phases. The unit cell of the  $1H$  phase is indicated by the red rhombus in (a), and that of the  $1T'$  phase is shown as a blue rectangle in (b). The Mo atoms are distorted from their original hexagonal positions to form 1D zigzag chains along the  $y$  axis in the  $1T'$  phase, shown by dashed black lines in (b). (c) The associated 2D Brillouin zones (BZs) with high-symmetry points marked. The  $K$  points of the hexagonal BZ (red) fold onto the  $\Gamma$ - $Y$  line of the  $1T'$  rectangular BZ (blue). (d) Phonon dispersion in  $1T'$ - $MoSi_2P_4$ . (e) Total free energy of monolayer  $1T'$ - $MoSi_2P_4$  as a function of time step during the molecular dynamics simulation at  $T = 300$  K.

phase. Figure 1(c) illustrates the BZs associated with both the  $1H$  and  $1T'$  phases, where high-symmetry points are marked in both the pristine hexagonal and reduced rectangular BZs.

To determine the stability of polytypic structures, we present the calculated phonon dispersion of monolayer  $1T'$ - $MoSi_2P_4$  in Fig. 1(d). The absence of imaginary frequency modes throughout the BZ indicates the dynamical stability of the  $1T'$  phase. The structural stability is further substantiated by performing *ab initio* molecular dynamics simulations at 300 K. Variation of the free energy as a function of the simulation time is presented in Fig. 1(e). The energy oscillates near a mean value of 6.40 eV/atom. However, the monolayer structure remains intact at the end of the simulations without any new reconstruction of the lattice, indicating thermal stability of the monolayer. We have also checked the thermodynamic stability of other members of the  $1T'$ - $MSi_2Z_4$  family and found them to be stable (see the Supplemental Material [50]). Like the experimentally realized  $1T'$  TMDs, these results indicate that  $1T'$ - $MSi_2Z_4$  is stable and it should be possible to synthesize it experimentally under appropriate chemical, thermal, or mechanical conditions [51,52]. On comparing the total energies of the  $1T'$ ,  $1H$ , and  $1T$  phases of  $MSi_2Z_4$ , we find that the  $1H$  phase is the most stable, followed by the  $1T'$  phase. The  $1T$  phase is unstable and relaxes to the  $1T'$  phase. The calculated energy difference between the  $1H$  and  $1T'$  phases is 55, 24, 47, and 11 meV/atom for  $MoSi_2P_4$ ,  $MoSi_2As_4$ ,  $WSi_2P_4$ , and  $WSi_2As_4$ , respectively. These results

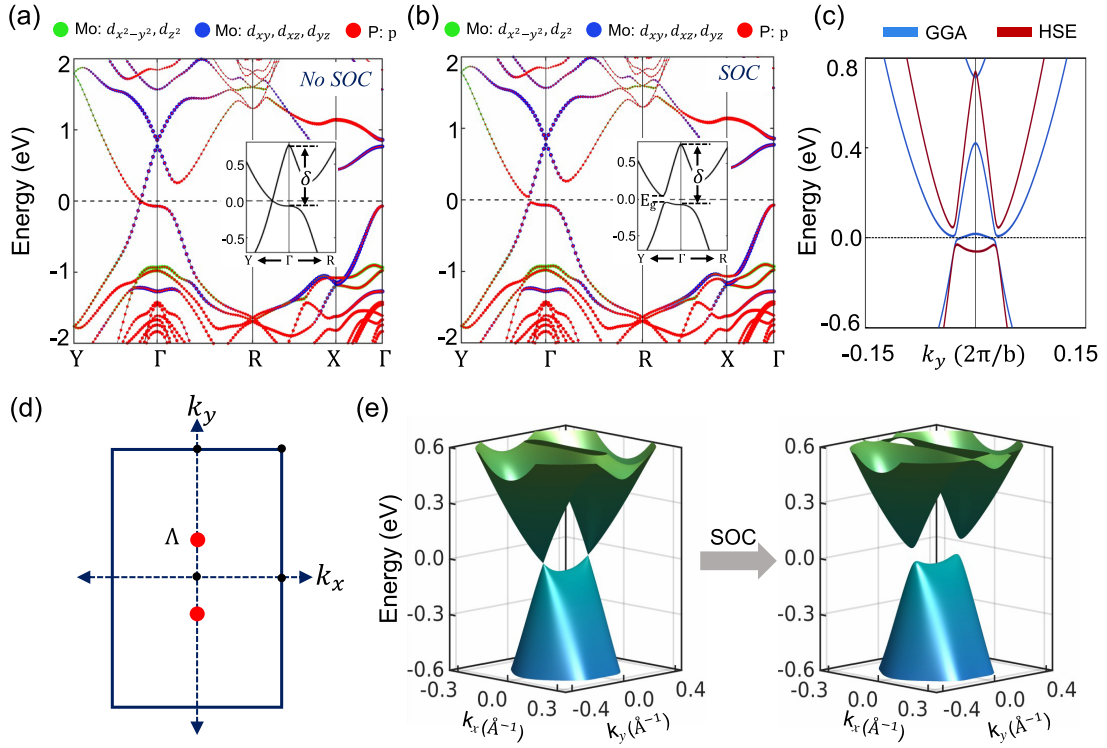


FIG. 2. Band structure of  $1T'$ - $\text{MoSi}_2\text{P}_4$  (a) without and (b) with spin-orbit coupling using the HSE hybrid functional. The horizontal dashed line marks the Fermi level. Orbital compositions of bands are shown using different colors. Insets show close-ups of bands near the  $\Gamma$  point at the Fermi level. The inverted band gap  $\delta$  and global band gap  $E_g$  are marked. (c) Close-ups of bands obtained with HSE and GGA functionals along the  $Y$ - $\Gamma$ - $Y$  line. (d) Location of valence and conduction band crossings at the Fermi level without spin-orbit coupling in the 2D Brillouin zone. (e)  $E$ - $k_x$ - $k_y$  space rendition of spin-orbit-coupling-driven electronic structure crossover in monolayer  $1T'$ - $\text{MoSi}_2\text{P}_4$  with the HSE functional.

indicate that the  $1T'$  phase can be realized under selective growth conditions, as has been done, for example, for the realization of the  $1T'$  phase of  $\text{MoS}_2$  [51,52].

### B. Bulk electronic structure and band inversion

We now discuss the orbital-resolved electronic structures computed with GGA and HSE functionals to delineate the topological states of various  $1T'$ - $\text{MSi}_2\text{Z}_4$  compounds. Figures 2(a) and 2(b) show representative HSE band structures of  $1T'$ - $\text{MSi}_2\text{Z}_4$ , taking  $\text{MoSi}_2\text{P}_4$  as an example. The band structure is semimetallic with isolated spinless Dirac-type crossings in the  $\Gamma$ - $Y$  directions without SOC [Fig. 2(a)]. Adding relativistic effects opens a hybridization gap at these band crossings, thereby realizing a semiconducting state with a global band gap  $E_g^{\text{HSE}}$  of 86 meV. The valence and conduction band extrema are located away from time-reversal-invariant momentum (TRIM) points at  $\Lambda = \pm 0.103 \text{ \AA}^{-1}$  [red dots in Fig. 2(d)] on the  $\Gamma$ - $Y$  line, forming a camelback-like band structure near the  $\Gamma$  point [53,54]. Such a band structure generally points to a nontrivial topology. We find that the  $p$  states of P lie below the Mo  $d$  states with a clear band inversion at the  $\Gamma$  point, strong hybridization between the P and Mo states notwithstanding. This unusual orbital ordering is driven by a structural transition from  $1H$  to  $1T'$ , which lowers the energy of the transition metal states and results in a large inverted band gap  $\delta^{\text{HSE}}$  of 842 meV at the  $\Gamma$  point that is larger than the existing  $1T'$  QSH materials.

(The inverted band gap  $\delta$  refers to the energy gap between the highest occupied P  $p$  and the lowest unoccupied Mo  $d$  states at the  $\Gamma$  point; see Fig. 2.) The calculated electronic and structural parameters for our investigated  $1T'$ - $\text{MSi}_2\text{Z}_4$  materials are listed in Table I, with band structures shown in the Supplemental Material. Since monolayer  $1T'$ - $\text{MSi}_2\text{Z}_4$  respects inversion symmetry, we calculated the  $Z_2$  invariant from the parity eigenvalues of the occupied states at the TRIM points and found  $Z_2 = 1$  (nontrivial) in all investigated materials. We thus predict the 2D  $1T'$ - $\text{MSi}_2\text{Z}_4$  monolayers are QSH insulators.

We present the band structures obtained using HSE06 (red curves) and GGA (blue curves) along the  $Y$ - $\Gamma$ - $Y$  directions in Fig. 2(c) to estimate the band gap corrections in  $1T'$ - $\text{MSi}_2\text{Z}_4$  monolayers. The hybrid functionals are generally considered to be more accurate in estimating band bending, band order, and band gap in comparison to the GGA. While the HSE06 is seen to correct the inverted band gap at the  $\Gamma$  point in comparison to the GGA, the overall band structures obtained with the two functionals are topologically equivalent to a band inversion at the  $\Gamma$  point. Figure 2(e) considers the formation of the QSH state in  $1T'$ - $\text{MSi}_2\text{Z}_4$  monolayers by switching off the SOC. Specifically, the gapless band crossings are found at finite momenta along the  $Y$ - $\Gamma$ - $Y$  line at the  $\Lambda$  points. Switching on the SOC hybridizes these band crossings to generate the QSH state. These results imply that the band inversion in 2D  $1T'$ - $\text{MSi}_2\text{Z}_4$  emerges via the structural transition, while the SOC is responsible for forming the QSH state.

TABLE I. Calculated structural and electronic parameters of 2D  $1T'$ - $MSi_2Z_4$  ( $M = \text{Mo}$  or  $\text{W}$  and  $Z = \text{P}$  or  $\text{As}$ ). The structural parameters include in-plane lattice constants  $a$  and  $b$  and the interatomic separations  $d_1$  and  $d_2$  in the transition-metal zigzag chain. The electronic parameters presented are the global band gaps obtained with GGA ( $E_g^{\text{GGA}}$ ) and HSE ( $E_g^{\text{HSE}}$ ) and the inverted band gaps at the  $\Gamma$  point calculated with GGA ( $\delta^{\text{GGA}}$ ) and HSE ( $\delta^{\text{HSE}}$ ). The topological state is indicated: QSH denotes the quantum spin Hall state. See text for details.

Material	$a$ (Å)	$b$ (Å)	$d_1$ (Å)	$d_2$ (Å)	Band gap (meV)		Inverted gap (meV)		Topological invariant	Topological state
					$E_g^{\text{GGA}}$	$E_g^{\text{HSE}}$	$\delta^{\text{GGA}}$	$\delta^{\text{HSE}}$	$Z_2$	
MoSi <sub>2</sub> P <sub>4</sub>	6.141	3.430	2.945	4.194	-10.4	86.2	398	842	1	QSH
MoSi <sub>2</sub> As <sub>4</sub>	6.388	3.579	3.012	4.362	-39.5	109.2	391	800	1	QSH
WSi <sub>2</sub> P <sub>4</sub>	6.129	3.441	2.939	4.133	-23.2	198.5	712	1079	1	QSH
WSi <sub>2</sub> As <sub>4</sub>	6.364	3.589	2.993	4.368	-0.07	204.3	675	1058	1	QSH

### C. Edge states and spin Hall conductivity

The appearance of spin-polarized edge states protected by the time-reversal symmetry is the hallmark of the QSH state. To highlight these states, we plot the calculated edge-state spectrum and the associated spin texture of MoSi<sub>2</sub>P<sub>4</sub> in Fig. 3. Figure 3(a) depicts the terminated left and right edges along the  $y$  axis with schematics of the nontrivial states of our  $xy$  monolayer ( $x$  remains the periodic direction). Since the two

edges are related by inversion symmetry, we display states for the left edge in Figs. 3(b) and 3(c). A pair of counterpropagating states with opposite spin polarization are seen in the band gap with a Dirac point at  $\bar{\Gamma}$ . The nontrivial edge states span the whole  $\bar{\Gamma}$ - $\bar{X}$  line to connect the bulk valence and conduction bands, as shown schematically in Fig. 3(e). Similar results are found for other  $1T'$ - $MSi_2Z_4$  materials.

Having established the QSH state in  $1T'$ - $MSi_2Z_4$  monolayers, we turn to discuss their intrinsic SHCs. We obtain the SHC  $\sigma_{xy}^z$  using the Kubo formula [55–59]:

$$\sigma_{xy}^z = \frac{-e^2}{\hbar} \frac{1}{A} \sum_{\mathbf{k}} \Omega_{xy}^z(\mathbf{k}), \quad (1)$$

where

$$\Omega_{xy}^z(\mathbf{k}) = \sum_n f_n(\mathbf{k}) \Omega_{n,xy}^z(\mathbf{k}) \quad (2)$$

is the  $k$ -resolved spin Berry curvature and

$$\Omega_{n,xy}^z(\mathbf{k}) = \hbar^2 \sum_{m \neq n} \frac{-2\text{Im}\langle n\mathbf{k} | \hat{f}_x^z | m\mathbf{k} \rangle \langle m\mathbf{k} | \hat{v}_y | n\mathbf{k} \rangle}{(E_{n\mathbf{k}} - E_{m\mathbf{k}})^2} \quad (3)$$

is the band-resolved spin Berry curvature.

In Eqs. (1)–(3),  $A$  is the area of the 2D unit cell, and  $|n\mathbf{k}\rangle$  denotes the Bloch state with energy  $E_{n\mathbf{k}}$  and occupation  $f_n(\mathbf{k})$ . The spin current operator  $\hat{f}_x^z = \frac{1}{2}\{\hat{\sigma}_z, \hat{v}_x\}$ , with  $\hat{\sigma}_z$  being the spin operator and  $\hat{v}_x$  being the velocity operator. The SHC  $\sigma_{x,y}^z$  represents the spin current along the  $x$  direction generated by the electric field along the  $y$  direction, where the spin current is polarized along the  $z$  direction. We used a dense grid of  $10^6$   $k$  points in conjunction with maximally localized Wannier functions to evaluate the spin Berry curvature and SHC. Figure 4(a) presents the calculated SHC as a function of the Fermi energy. The SHC is maximum near the band-crossing points (marked by the dashed line), reaching a value of  $\sim 1.3 \frac{e^2}{\hbar}$ , which is much larger than the  $1T'$  TMDs with the QSH state. The amplitude of the SHC decreases quickly away from the band-crossing points. This can be further seen from our band- and  $k$ -resolved spin Berry curvature in Fig. 4(b). The spin Berry curvature is largely concentrated near the valence and conduction band-crossing points along the  $\Gamma$ - $Y$  direction, which have a SOC-driven hybridization gap. Notably, the perfect quantization of the SHC requires an  $S_z$ -conserved Hamiltonian. However, realistic material parameters depend on the constraints of point-group symmetries, coupling of

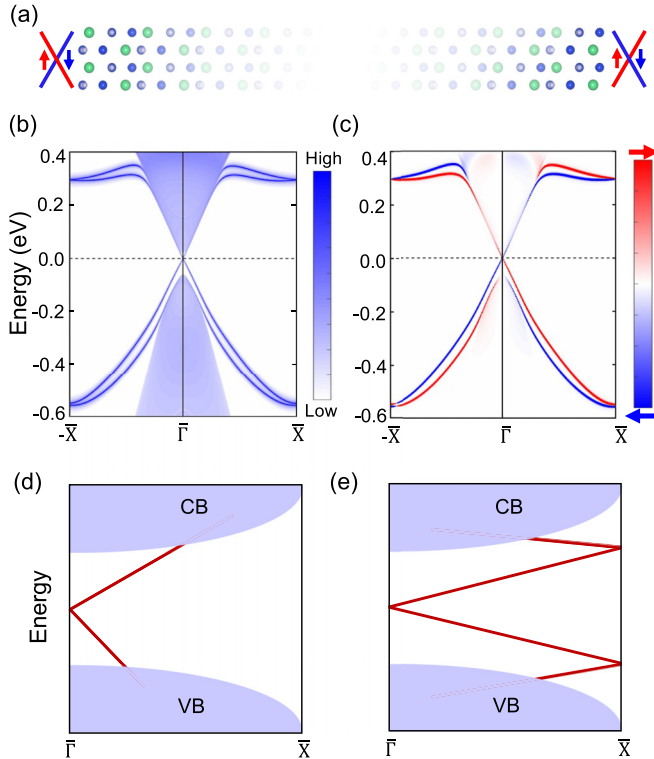


FIG. 3. (a) Lattice structure of semi-infinite one-dimensional edges of  $1T'$ -MoSi<sub>2</sub>P<sub>4</sub>. Spin-polarized edge states are shown schematically on the left and right edges. (b) Electronic spectrum of the (010) edge. Nontrivial edge states can be seen in the 2D bulk band gap. (c) Calculated left edge state's spin texture in 2D  $1T'$ -MoSi<sub>2</sub>P<sub>4</sub>. Red (blue) indicates up (down) spin polarization. (d) and (e) Schematic representations of the various nontrivial edge states (red lines) connecting the bulk valence and conduction bands (light blue shading) between the two time-reversal-invariant points  $\bar{\Gamma}$  and  $\bar{X}$ .

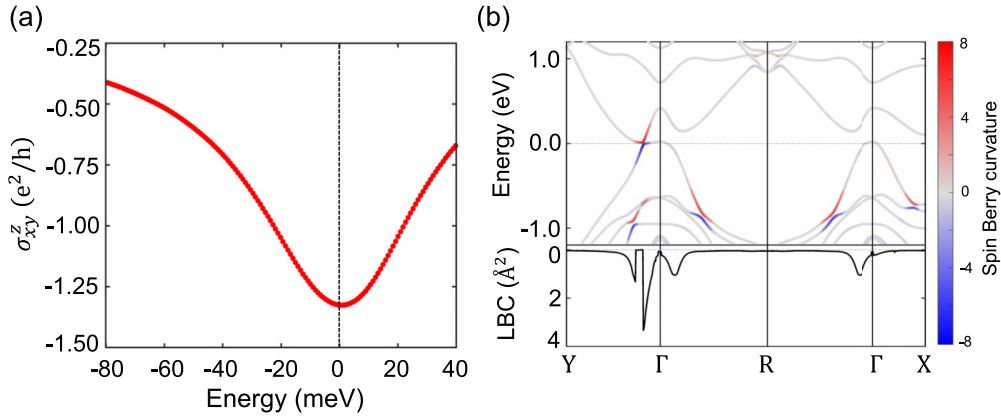


FIG. 4. (a) Intrinsic spin Hall conductivity (SHC)  $\sigma_{xy}^z$  as a function of Fermi energy in monolayer  $1T'$ - $\text{MoSi}_2\text{P}_4$ . SHC is given in units of  $\frac{e^2}{h}$ . The value of the SHC is maximum at the Fermi level. (b) Band-resolved (top) and  $k$ -resolved (bottom) spin Berry curvature of monolayer  $\text{MoSi}_2\text{P}_4$  along the high-symmetry directions in the 2D Brillouin zone. LBC stands for the logarithm of  $\Omega_{xy}^z(\mathbf{k})$  [Eq. (2)], and the color bar refers to the logarithm of  $\Omega_{n,xy}^z(\mathbf{k})$  [Eq. (3)].

various bands, and the local atomic geometries, among other factors, which lead to nonconserved- $S_z$  Hamiltonians [60]. As the local atomic geometry and spin-orbit interactions in  $\text{MSi}_2\text{Z}_4$  are different from the  $1T'$  TMDs, differences in their SHC values are naturally expected [61]. An optimal setup to exploit the large SHC in  $\text{MoSi}_2\text{P}_4$  would be in the clean limit with the Fermi level lying between the band-crossing points.

#### D. Electric field switching of the quantum spin Hall state

We now demonstrate the tunability of the QSH state and the switching of the topological state under a vertical electric field. Topologically inverted bands between the transition metal  $d$  and pnictogen's  $p$  orbitals lie in well-separated 2D planes in the  $1T'$  monolayer. This distinct spatial location of bands provides a natural basis for their tunability via an out-of-plane (vertical) electric field  $E_z$ . Figure 5 shows the HSE band structure for various electric field values. The electric field induces Rashba spin splittings in the states by breaking the inversion equivalence on the top and bottom sides of the monolayers. This is evident from spin-split states shown with distinct colors in the top panels of Figs. 5(b) and 5(c). As the electric field increases, the band gap decreases to zero at the critical electric field value of  $E_c = 0.187 \text{ eV/\AA}$ , where the spin-up and spin-down bands cross at opposite  $\Lambda$  points. With a further increase in the electric field, the band gap reopens. An analysis based on the  $Z_2$  invariants and edge-state dispersions (Fig. 5) shows that this band gap closing drives a change in the topology to a trivial state with  $Z_2 = 0$ . This topological phase transition destroys the topological edge states, thereby switching off the QSH state in  $1T'$ - $\text{MoSi}_2\text{P}_4$ . A change in the polarity of the electric field shows a similar topological phase transition to a trivial state. The evolution of the QSH and trivial insulator states as a function of the applied electric field is displayed in Fig. 6.

The preceding results indicate an electric field on-off control of the spin-polarized edge currents in  $1T'$ - $\text{MSi}_2\text{Z}_4$  similar to the case of  $1T'$  TMDs [14]. Since the crystal symmetries of both these material families are the same, various device ideas conceived for  $1T'$  TMDs can be applied to the  $\text{MSi}_2\text{Z}_4$

family with the added advantage of a large, inverted band gap and large SHC. For example, monolayer  $\text{MSi}_2\text{Z}_4$  could be interfaced with a large band gap 2D insulator to protect the helical edge channels from being gapped by interlayer hybridization to realize a topological transistor [14]. When the Fermi level is placed in the nontrivial band gap, a nearly quantized SHC would be realized in this device under zero or small electric fields. An electric field beyond the critical value of  $\pm 0.187 \text{ eV/\AA}$  can switch off the quantized spin Hall conductance, driving it into a trivial insulating state.

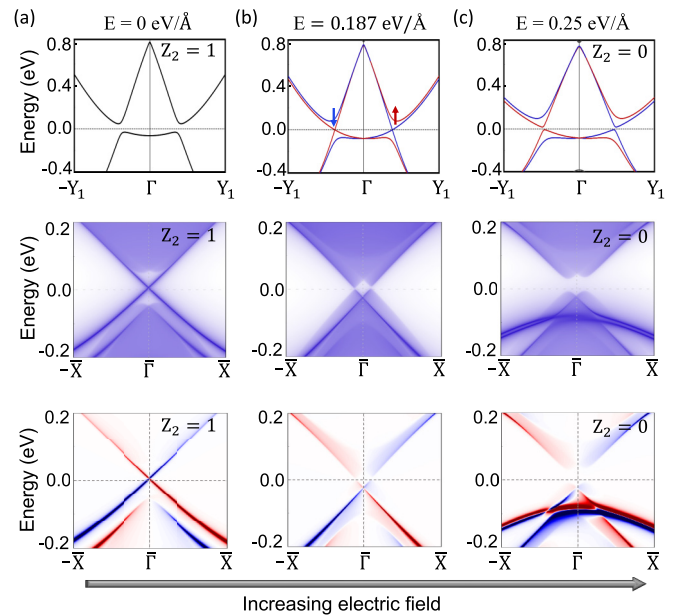


FIG. 5. Band structure of the  $1T'$ - $\text{MoSi}_2\text{P}_4$  monolayer for various values of the vertical electric field  $E_z$ : (a) 0, (b) 0.187, and (c) 0.250  $\text{eV/\AA}$ . The top, middle, and bottom rows show the 2D band structure, the (010) edge spectrum, and the edge-state spin texture, respectively. Red (blue) identifies the up (down) spin state.

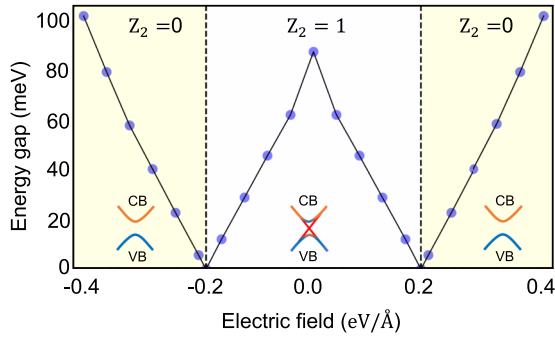


FIG. 6. Topological phase diagram of  $1T'$ - $\text{MoSi}_2\text{P}_4$  as a function of the vertical electric field  $E_z$ . Critical electric field strengths for the topological phase transition from the  $Z_2 = 1$  to  $Z_2 = 0$  state are marked by vertical dashed lines.

#### IV. SUMMARY

We have demonstrated the existence of a tunable QSH state with a large band gap in a polytypic structure of the recently introduced bottom-up synthesized  $\text{MSi}_2\text{Z}_4$  family of 2D materials. Our analysis based on phonon spectra and molecular dynamics simulations showed that these materials realize a thermodynamically stable  $1T'$  phase in addition to the putative  $1H$  phase. Our in-depth electronic structure modeling revealed that a structural distortion in the  $1H$  phase leads to the  $1T'$  structure and induces a topological band inversion. A hybridization gap as large as 204 meV was found for the  $\text{MSi}_2\text{Z}_4$  family that is even larger than the one in the existing  $1T'$  TMDs that host a QSH ground state. Our calculated SHC shows a large value of  $\sim 1.3 \frac{e^2}{h}$  in  $\text{MoSi}_2\text{P}_4$  that arises from the large spin Berry curvature induced by spin-orbit-split bands at the band inversion points. We also showed that the QSH

state is tunable with a vertical electric field, which provides an external control for switching or turning on and off the QSH state. Our study thus not only introduces a polytypic structure of the recently introduced 2D  $\text{MSi}_2\text{Z}_4$  materials, which support a large band gap QSH state, but also suggests that this material family will potentially provide a promising platform for realizing nontrivial states with large spin Hall conductance.

#### ACKNOWLEDGMENTS

This work is supported by the Department of Atomic Energy of the government of India under Project No. 12-R&D-TFR-5.10-0100. The work at the Institute of Physics, Polish Academy of Sciences, is supported by the Foundation for Polish Science through the International Research Agendas program cofinanced by the European Union within the Smart Growth Operational Programme and the National Science Center in the framework of the “PRELUDIUM” (Decision No. DEC-2020/37/N/ST3/02338). We acknowledge the access to the computing facilities of the Interdisciplinary Center of Modeling at the University of Warsaw, Grants No. G84-0, No. GB84-1, and No. GB84-7. We acknowledge the CINECA award under the ISCRA initiative IsC93 “RATIO” and IsC99 “SILENTS” grant for the availability of high-performance computing resources and support. Z.M. acknowledges the support by the National Natural Science Foundation of China under Grant No. 62150410438. The work at Northeastern University was supported by the Air Force Office of Scientific Research under Award No. FA9550-20-1-0322, and it benefited from the computational resources of Northeastern University’s Advanced Scientific Computation Center (ASCC) and the Discovery Cluster.

- [1] K. S. Novoselov, Nobel lecture: Graphene: Materials in the flatland, *Rev. Mod. Phys.* **83**, 837 (2011).
- [2] A. H. Castro Neto, F. Guinea, N. M. R. Peres, K. S. Novoselov, and A. K. Geim, The electronic properties of graphene, *Rev. Mod. Phys.* **81**, 109 (2009).
- [3] K. S. Novoselov, D. Jiang, F. Schedin, T. J. Booth, V. V. Khotkevich, S. V. Morozov, and A. K. Geim, Two-dimensional atomic crystals, *Proc. Natl. Acad. Sci. USA* **102**, 10451 (2005).
- [4] S. Manzeli, D. Ovchinnikov, D. Pasquier, O. V. Yazyev, and A. Kis, 2D transition metal dichalcogenides, *Nat. Rev. Mater.* **2**, 17033 (2017).
- [5] C. L. Kane and E. J. Mele, Quantum Spin Hall Effect in Graphene, *Phys. Rev. Lett.* **95**, 226801 (2005).
- [6] C. L. Kane and E. J. Mele,  $Z_2$  Topological Order and the Quantum Spin Hall Effect, *Phys. Rev. Lett.* **95**, 146802 (2005).
- [7] A. Bansil, H. Lin, and T. Das, Colloquium: Topological band theory, *Rev. Mod. Phys.* **88**, 021004 (2016).
- [8] M. Z. Hasan and C. L. Kane, Colloquium: Topological insulators, *Rev. Mod. Phys.* **82**, 3045 (2010).
- [9] B. Singh, H. Lin, and A. Bansil, Topology and symmetry in quantum materials, *Adv. Mater.*, 2201058 (2022).
- [10] B. A. Bernevig and S.-C. Zhang, Quantum Spin Hall Effect, *Phys. Rev. Lett.* **96**, 106802 (2006).
- [11] B. A. Bernevig, T. L. Hughes, and S.-C. Zhang, Quantum spin Hall effect and topological phase transition in HgTe quantum wells, *Science* **314**, 1757 (2006).
- [12] B. Singh, H. Lin, R. Prasad, and A. Bansil, Topological phase transition and two-dimensional topological insulators in Ge-based thin films, *Phys. Rev. B* **88**, 195147 (2013).
- [13] A. Marrazzo, M. Gibertini, D. Campi, N. Mounet, and N. Marzari, Prediction of a Large-Gap and Switchable Kane-Mele Quantum Spin Hall Insulator, *Phys. Rev. Lett.* **120**, 117701 (2018).
- [14] X. Qian, J. Liu, L. Fu, and J. Li, Quantum spin Hall effect in two-dimensional transition metal dichalcogenides, *Science* **346**, 1344 (2014).
- [15] Y. Xu, B. Yan, H.-J. Zhang, J. Wang, G. Xu, P. Tang, W. Duan, and S.-C. Zhang, Large-Gap Quantum Spin Hall Insulators in Tin Films, *Phys. Rev. Lett.* **111**, 136804 (2013).
- [16] C. Liu, T. L. Hughes, X.-L. Qi, K. Wang, and S.-C. Zhang, Quantum Spin Hall Effect in Inverted Type-II Semiconductors, *Phys. Rev. Lett.* **100**, 236601 (2008).
- [17] M. König, S. Wiedmann, C. Brüne, A. Roth, H. Buhmann, L. W. Molenkamp, X.-L. Qi, and S.-C. Zhang, Quantum spin Hall insulator state in HgTe quantum wells, *Science* **318**, 766 (2007).

- [18] I. Knez, R.-R. Du, and G. Sullivan, Evidence for Helical Edge Modes in Inverted InAs/GaSb Quantum Wells, *Phys. Rev. Lett.* **107**, 136603 (2011).
- [19] S. Tang, C. Zhang, D. Wong, Z. Pedramrazi, H.-Z. Tsai, C. Jia, B. Moritz, M. Claassen, H. Ryu, S. Kahn *et al.*, Quantum spin Hall state in monolayer  $1T'$ -WTe<sub>2</sub>, *Nat. Phys.* **13**, 683 (2017).
- [20] K. Kandrai, P. Vancsó, G. Kukucska, J. Koltai, G. Baranka, Á. Hoffmann, Á. Pekker, K. Kamarás, Z. E. Horváth, A. Vymazalová, L. Tapasztó, and P. Nemes-Incze, Signature of large-gap quantum spin Hall state in the layered mineral jacutingaite, *Nano Lett.* **20**, 5207 (2020).
- [21] N. Shumiya *et al.*, Evidence of a room-temperature quantum spin Hall edge state in a higher-order topological insulator, *Nat. Mater.* **21**, 1111 (2022).
- [22] Z. Fei, T. Palomaki, S. Wu, W. Zhao, X. Cai, B. Sun, P. Nguyen, J. Finney, X. Xu, and D. H. Cobden, Edge conduction in monolayer WTe<sub>2</sub>, *Nat. Phys.* **13**, 677 (2017).
- [23] S. Wu, V. Fatemi, Q. D. Gibson, K. Watanabe, T. Taniguchi, R. J. Cava, and P. Jarillo-Herrero, Observation of the quantum spin Hall effect up to 100 kelvin in a monolayer crystal, *Science* **359**, 76 (2018).
- [24] H. Lin, R. S. Markiewicz, L. A. Wray, L. Fu, M. Z. Hasan, and A. Bansil, Single-Dirac-Cone Topological Surface States in the TLBiSe<sub>2</sub> Class of Topological Semiconductors, *Phys. Rev. Lett.* **105**, 036404 (2010).
- [25] Y.-F. Zhang, J. Pan, H. Banjade, J. Yu, H. Lin, A. Bansil, S. Du, and Q. Yan, Two-dimensional MX Dirac materials and quantum spin Hall insulators with tunable electronic and topological properties, *Nano Res.* **14**, 584 (2021).
- [26] Z.-Y. Jia, Y.-H. Song, X.-B. Li, K. Ran, P. Lu, H.-J. Zheng, X.-Y. Zhu, Z.-Q. Shi, J. Sun, J. Wen, D. Xing, and S.-C. Li, Direct visualization of a two-dimensional topological insulator in the single-layer  $1T'$ -WTe<sub>2</sub>, *Phys. Rev. B* **96**, 041108(R) (2017).
- [27] Z. Li, Y. Song, and S. Tang, Quantum spin Hall state in monolayer  $1T'$ -TMDCs, *J. Phys.: Condens. Matter* **32**, 333001 (2020).
- [28] Y. Cao *et al.*, Quality heterostructures from two-dimensional crystals unstable in air by their assembly in inert atmosphere, *Nano Lett.* **15**, 4914 (2015).
- [29] Y. Zhang, K. He, C.-Z. Chang, C.-L. Song, L.-L. Wang, X. Chen, J.-F. Jia, Z. Fang, X. Dai, W.-Y. Shan, S.-Q. Shen, Q. Niu, X.-L. Qi, S.-C. Zhang, X.-C. Ma, and Q.-K. Xue, Crossover of the three-dimensional topological insulator Bi<sub>2</sub>Se<sub>3</sub> to the two-dimensional limit, *Nat. Phys.* **6**, 584 (2010).
- [30] F. Ye, J. Lee, J. Hu, Z. Mao, J. Wei, and P. X.-L. Feng, Environmental instability and degradation of single- and few-layer WTe<sub>2</sub> nanosheets in ambient conditions, *Small* **12**, 5802 (2016).
- [31] J.-J. Zhang, D. Zhu, and B. I. Yakobson, Heterobilayer with ferroelectric switching of topological state, *Nano Lett.* **21**, 785 (2021).
- [32] K. S. Novoselov, A. Mishchenko, A. Carvalho, and A. H. C. Neto, 2D materials and van der Waals heterostructures, *Science* **353**, aac9439 (2016).
- [33] K. S. Novoselov, Discovery of 2D van der Waals layered MoSi<sub>2</sub>N<sub>4</sub> family, *Natl. Sci. Rev.* **7**, 1842 (2020).
- [34] Y.-L. Hong, Z. Liu, L. Wang, T. Zhou, W. Ma, C. Xu, S. Feng, L. Chen, M.-L. Chen, D.-M. Sun *et al.*, Chemical vapor deposition of layered two-dimensional MoSi<sub>2</sub>N<sub>4</sub> materials, *Science* **369**, 670 (2020).
- [35] R. Islam, B. Ghosh, C. Autieri, S. Chowdhury, A. Bansil, A. Agarwal, and B. Singh, Tunable spin polarization and electronic structure of bottom-up synthesized MoSi<sub>2</sub>N<sub>4</sub> materials, *Phys. Rev. B* **104**, L201112 (2021).
- [36] C. Yang, Z. Song, X. Sun, and J. Lu, Valley pseudospin in monolayer MoSi<sub>2</sub>N<sub>4</sub> and MoSi<sub>2</sub>As<sub>4</sub>, *Phys. Rev. B* **103**, 035308 (2021).
- [37] S. Li, W. Wu, X. Feng, S. Guan, W. Feng, Y. Yao, and S. A. Yang, Valley-dependent properties of monolayer MoSi<sub>2</sub>N<sub>4</sub>, WSi<sub>2</sub>N<sub>4</sub>, and MoSi<sub>2</sub>As<sub>4</sub>, *Phys. Rev. B* **102**, 235435 (2020).
- [38] X. Feng, X. Xu, Z. He, R. Peng, Y. Dai, B. Huang, and Y. Ma, Valley-related multiple Hall effect in monolayer VSi<sub>2</sub>P<sub>4</sub>, *Phys. Rev. B* **104**, 075421 (2021).
- [39] S. Bertolazzi, J. Brivio, and A. Kis, Stretching and breaking of ultrathin MoS<sub>2</sub>, *ACS Nano* **5**, 9703 (2011).
- [40] Y. Cai, G. Zhang, and Y.-W. Zhang, Polarity-reversed robust carrier mobility in monolayer MoS<sub>2</sub> nanoribbons, *J. Am. Chem. Soc.* **136**, 6269 (2014).
- [41] P. Hohenberg and W. Kohn, Inhomogeneous electron gas, *Phys. Rev.* **136**, B864 (1964).
- [42] G. Kresse and J. Furthmüller, Efficient iterative schemes for *ab initio* total-energy calculations using a plane-wave basis set, *Phys. Rev. B* **54**, 11169 (1996).
- [43] J. P. Perdew, K. Burke, and M. Ernzerhof, Generalized Gradient Approximation Made Simple, *Phys. Rev. Lett.* **77**, 3865 (1996).
- [44] J. Heyd, G. E. Scuseria, and M. Ernzerhof, Hybrid functionals based on a screened Coulomb potential, *J. Chem. Phys.* **118**, 8207 (2003).
- [45] A. Togo and I. Tanaka, First principles phonon calculations in materials science, *Scr. Mater.* **108**, 1 (2015).
- [46] R. N. Barnett and U. Landman, Born-Oppenheimer molecular-dynamics simulations of finite systems: Structure and dynamics of (H<sub>2</sub>O)<sub>2</sub>, *Phys. Rev. B* **48**, 2081 (1993).
- [47] A. A. Mostofi, J. R. Yates, Y.-S. Lee, I. Souza, D. Vanderbilt, and N. Marzari, WANNIER90: A tool for obtaining maximally-localised Wannier functions, *Comput. Phys. Commun.* **178**, 685 (2008).
- [48] Q. Wu, S. Zhang, H.-F. Song, M. Troyer, and A. A. Soluyanov, WannierTools: An open-source software package for novel topological materials, *Comput. Phys. Commun.* **224**, 405 (2018).
- [49] M. P. L. Sancho, J. M. L. Sancho, J. M. L. Sancho, and J. Rubio, Highly convergent schemes for the calculation of bulk and surface Green functions, *J. Phys. F* **15**, 851 (1985).
- [50] See Supplemental Material at <http://link.aps.org/supplemental/10.1103/PhysRevB.106.245149> for the stability of  $1T'$ -MSi<sub>2</sub>Z<sub>4</sub> and bulk and edge-state properties for all the studied materials (see also Refs. [62–66] therein).
- [51] M. Calandra, Chemically exfoliated single-layer MoS<sub>2</sub>: Stability, lattice dynamics, and catalytic adsorption from first principles, *Phys. Rev. B* **88**, 245428 (2013).
- [52] L. Liu, J. Wu, L. Wu, M. Ye, X. Liu, Q. Wang, S. Hou, P. Lu, L. Sun, J. Zheng, L. Xing, L. Gu, X. Jiang, L. Xie, and L. Jiao, Phase-selective synthesis of  $1T'$ -MoS<sub>2</sub> monolayers and heterophase bilayers, *Nat. Mater.* **17**, 1108 (2018).
- [53] R. Islam, B. Ghosh, G. Cuono, A. Lau, W. Brzezicki, A. Bansil, A. Agarwal, B. Singh, T. Dietl, and C. Autieri, Topological states in superlattices of HgTe class of materials for engineering three-dimensional flat bands, *Phys. Rev. Res.* **4**, 023114 (2022).

- [54] G. Hussain, A. Samad, M. Ur Rehman, G. Cuono, and C. Autieri, Emergence of Rashba splitting and spin-valley properties in Janus MoGeSiP<sub>2</sub>As<sub>2</sub> and WGeSiP<sub>2</sub>As<sub>2</sub> monolayers, *J. Magn. Magn. Mater.* **563**, 169897 (2022).
- [55] L. Matthes, S. Küfner, J. Furthmüller, and F. Bechstedt, Intrinsic spin Hall conductivity in one-, two-, and three-dimensional trivial and topological systems, *Phys. Rev. B* **94**, 085410 (2016).
- [56] Y. Sun, Y. Zhang, C. Felser, and B. Yan, Strong Intrinsic Spin Hall Effect in the TaAs Family of Weyl Semimetals, *Phys. Rev. Lett.* **117**, 146403 (2016).
- [57] R. Zhang, C.-Y. Huang, J. Kidd, R. S. Markiewicz, H. Lin, A. Bansil, B. Singh, and J. Sun, Weyl semimetal in the rare-earth hexaboride family supporting a pseudonodal surface and a giant anomalous Hall effect, *Phys. Rev. B* **105**, 165140 (2022).
- [58] J. Zhou, J. Qiao, A. Bournel, and W. Zhao, Intrinsic spin Hall conductivity of the semimetals MoTe<sub>2</sub> and WTe<sub>2</sub>, *Phys. Rev. B* **99**, 060408(R) (2019).
- [59] J. Qiao, J. Zhou, Z. Yuan, and W. Zhao, Calculation of intrinsic spin Hall conductivity by Wannier interpolation, *Phys. Rev. B* **98**, 214402 (2018).
- [60] F. Matusalem, M. Marques, L. K. Teles, L. Matthes, J. Furthmüller, and F. Bechstedt, Quantization of spin Hall conductivity in two-dimensional topological insulators versus symmetry and spin-orbit interaction, *Phys. Rev. B* **100**, 245430 (2019).
- [61] Understanding the mechanisms responsible for large SHCs in MSi<sub>2</sub>Z<sub>4</sub> compared to TMDs would be interesting, but that requires an in-depth comparison of their geometric and electronic properties, which is outside the scope of this study.
- [62] A. A. Soluyanov and D. Vanderbilt, Computing topological invariants without inversion symmetry, *Phys. Rev. B* **83**, 235401 (2011).
- [63] A. Alexandradinata, X. Dai, and B. A. Bernevig, Wilson-loop characterization of inversion-symmetric topological insulators, *Phys. Rev. B* **89**, 155114 (2014).
- [64] R. Yu, X. L. Qi, A. Bernevig, Z. Fang, and X. Dai, Equivalent expression of  $\mathbb{Z}_2$  topological invariant for band insulators using the non-Abelian Berry connection, *Phys. Rev. B* **84**, 075119 (2011).
- [65] A. Bouhon and A. M. Black-Schaffer, Global band topology of simple and double Dirac-point semimetals, *Phys. Rev. B* **95**, 241101(R) (2017).
- [66] C. Autieri, A. Bouhon, and B. Sanyal, Gap opening and large spin-orbit splitting in MX<sub>2</sub> (M = Mo, W; X = S, Se, Te) from the interplay between crystal field and hybridisations insights from *ab-initio* theory, *Philos. Mag.* **97**, 3381 (2017).